

Supplementary Material

Trends and rhythms of carbonatite and kimberlite reflect thermal–tectonic evolution of Earth

Shuang-Liang Liu, Lin Ma, Xinyu Zou, Linru Fang, Ben Qin, Aleksey E. Melnik, Uwe Kirscher, Kui-Feng Yang, Hong-Rui Fan, and Ross N. Mitchell

This file contains:

Supplementary methods

Supplementary figures (Figs. S1–S7)

Supplementary references

Supplementary table (Provided a separate Excel spreadsheet named Table S1)

Filtering and updating of carbonatite age data

We updated the carbonatite age data following the iterative rules listed below, which are also provided as a workflow diagram in [Fig. S1](#).

(1) For a carbonatite occurrence, we select its magmatic age rather than its mineralization age, because the mineralization age may be controversial (e.g., Bayan Obo Fe-Nb-REE carbonatite related deposit; [Yang et al., 2019](#); [Li et al., 2021](#)).

(2) We use the latest high-quality radiometric geochronology to update the carbonatite database of [Woolley and Kjarsgaard \(2008\)](#).

(3) When no new age data are available, we adopt the age of [Woolley and Kjarsgaard \(2008\)](#), except for when the age of Woolley and Kjarsgaard is an “average” age. Here, we revise such average ages by the following rules below.

(a) Only ages that are published and have errors less than 40 m.y. are used.

(b) If there is only one individual age directly from carbonatite, this age will be adopted. If there is more than one individual age directly from carbonatite, we will select the optimal age according to an assessment of the relative reliability of the geochronology references. Otherwise, the revising procedure for an average age will follow (c).

(c) If the available ages from the same location are consistent within the range of age errors, the “average age” will still be used. Otherwise, if the ages are consistent within 40 m.y., the age data will be expressed by an age range, and the average age of that range will be used for the age frequency distribution. If the ages are not consistent within 40 m.y., these data are excluded from our age distribution analysis.

Data distributions

In [Figs. 2](#) and [S3](#), we show age distributions according to various bin size options from

40 m.y. (shorter than the short bandwidth range of the 400–800 m.y. period of supercontinent cycle) to 400 m.y. (half of the long bandwidth range of the 400–800 m.y. period of the supercontinent cycle). Distribution curves are evaluated by Loess (Locally estimated scatterplot) method and 10,000 bootstrap simulations in Acycle software (Li et al., 2019).

Trend fitting of data

The trends of the age frequency distributions are fitted by power law functions:

$$y = a(x - b)^c \quad (1)$$

The fitting model is evaluated by r^2 , which is calculated by the following equations:

$$\bar{y} = \frac{1}{n} \sum_{i=1}^n y_i \quad (2)$$

$$SS_{tot} = \sum_i (y_i - \bar{y})^2 \quad (3)$$

$$SS_{res} = \sum_i (y_i - f_i)^2 \quad (4)$$

$$r^2 = 1 - \frac{SS_{res}}{SS_{tot}} \quad (5)$$

where n is the number of observations in the fitting model, y_i is the observed value, and f_i is the fitted value.

Detrending

To eliminate the long-term trends and focus on the fluctuations of the data, the trend curve value (f_i) is subtracted from the corresponding value (y_i) of the distribution curve:

$$y_d = y_i - f_i \quad (6)$$

Lead-lag relationship

A lead-lag describes the situation where one (leading) variable is cross-correlated with the values of another (lagging) variable at later times. Here, we use the root mean square error (RMSE) to evaluate the cross-correlation between two time series, considering the non-normal distribution of them.

The procedure is as follows. (1) Fix kimberlite series as the reference ones in the coordinate system and shift carbonatite series along the horizontal axis, using the bin size as the step size. (2) Calculate the RMSE of these two sequences at each move. The translation corresponding to the minimum value of RMSE is the lead-lag time of the two time series.

Therefore, in this case, the positive lead-lag time value means the kimberlite time series lead the carbonatite ones, while the negative values have the opposite meaning.

Multi-taper method (MTM) spectral analysis

MTM power spectra compared robust first-order autoregressive “AR(1)” red noise models (Mann and Lees, 1996) are calculated in Acycle software (Li et al., 2019).

Monte Carlo simulation

The Monte Carlo method combined with the MTM method is performed to address the effect of the uncertainty of the estimated distribution curve on the results of the spectral analysis (i.e., periodic rhythms). The estimated curve exhibits periodic peaks in the 400–800 Myr range above the 90% confidence level. First, we randomly sampled the age distribution curve 10,000 times within a 1σ confidence interval. Second, we detrend their secular trend using the rLoess (robust Locally estimated scatterplot Regression) smoothing method with a span of 99%, which assigns zero weight to data outside of six standard deviations of the mean. We performed the non-parametric regression method instead of a power function to avoid the situation of a few extreme random values causing the parametric regression to fail to converge. Third, we calculate their power spectra using MTM, and note the peaks above the 90% confidence level. The calculated results are shown as violin plots containing kernel density plots and box plots with medium, interquartile ranges (IQR) and 1.5 times IQR. Statistics are cut off by corresponding frequency values of triple the bin size because the cycle of less than triple bin size should be meaningless. All calculations are coded and performed in Matlab and Acycle software (Li et al., 2019).

Sensitivity test of bin size selection

In order to test whether our results were dependent or independent of bin size selection, we conducted a sensitivity test of bin size selection across a wide range (40–400 m.y.). The test addresses the influence of bin size selection on the secular age distribution patterns, the similarity in the fluctuations, and the potential dominant periodicities of these two rocks (Figs. 2 and 3 for 40 m.y. bins; Figs. S3 and S4 for bin sizes ranging from 80–400 m.y.). Ultimately, the sensitivity test supports the secular trend and spectral analysis are robust and argues that our periodicity results are independent of bin size selection, within a reasonable range, i.e., not too long to over-smooth the potential periodic signals of interest and not too short to introduce high-frequency signals that are either noise or real signals that may or may not be present in the whole records, particularly during older intervals not as densely sampled as the past 200 m.y.

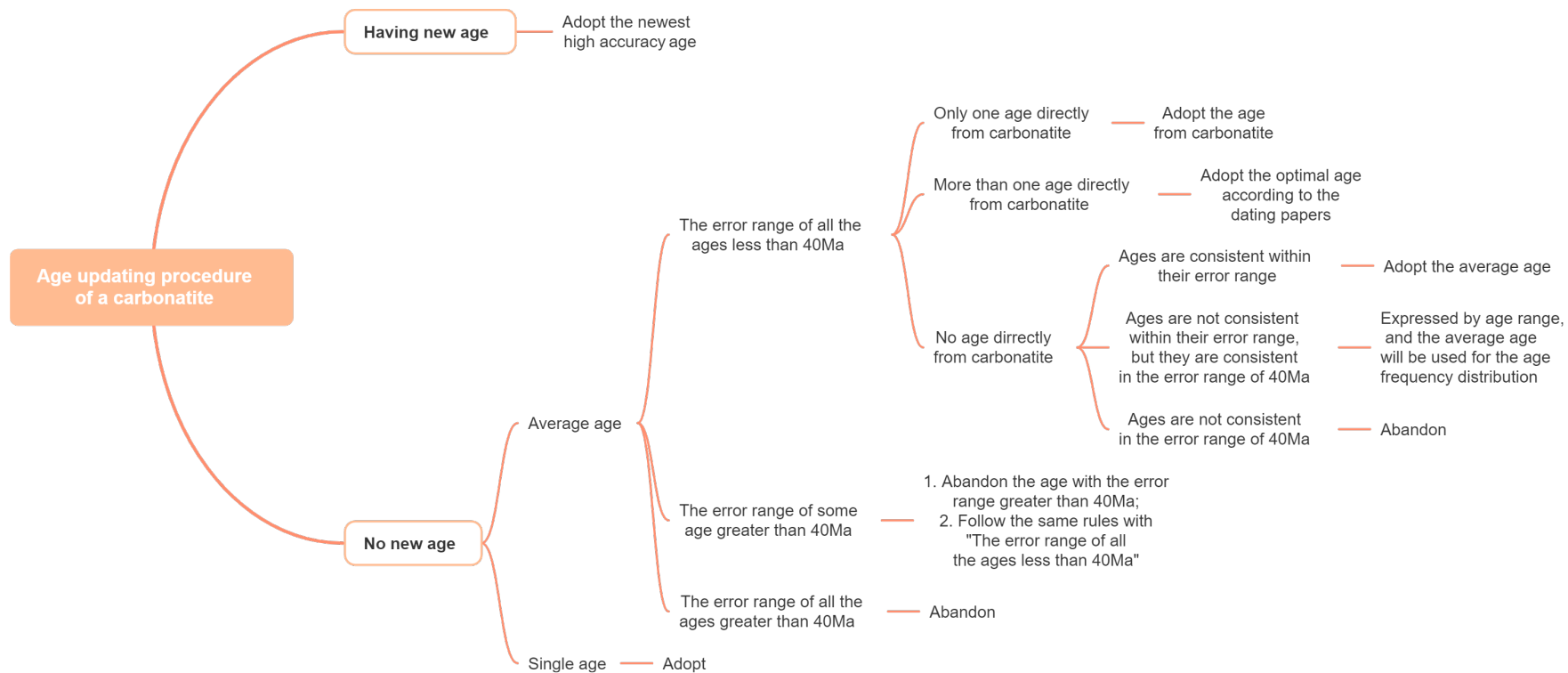


Fig. S1 Procedure for updating the ages of carbonatite occurrences.

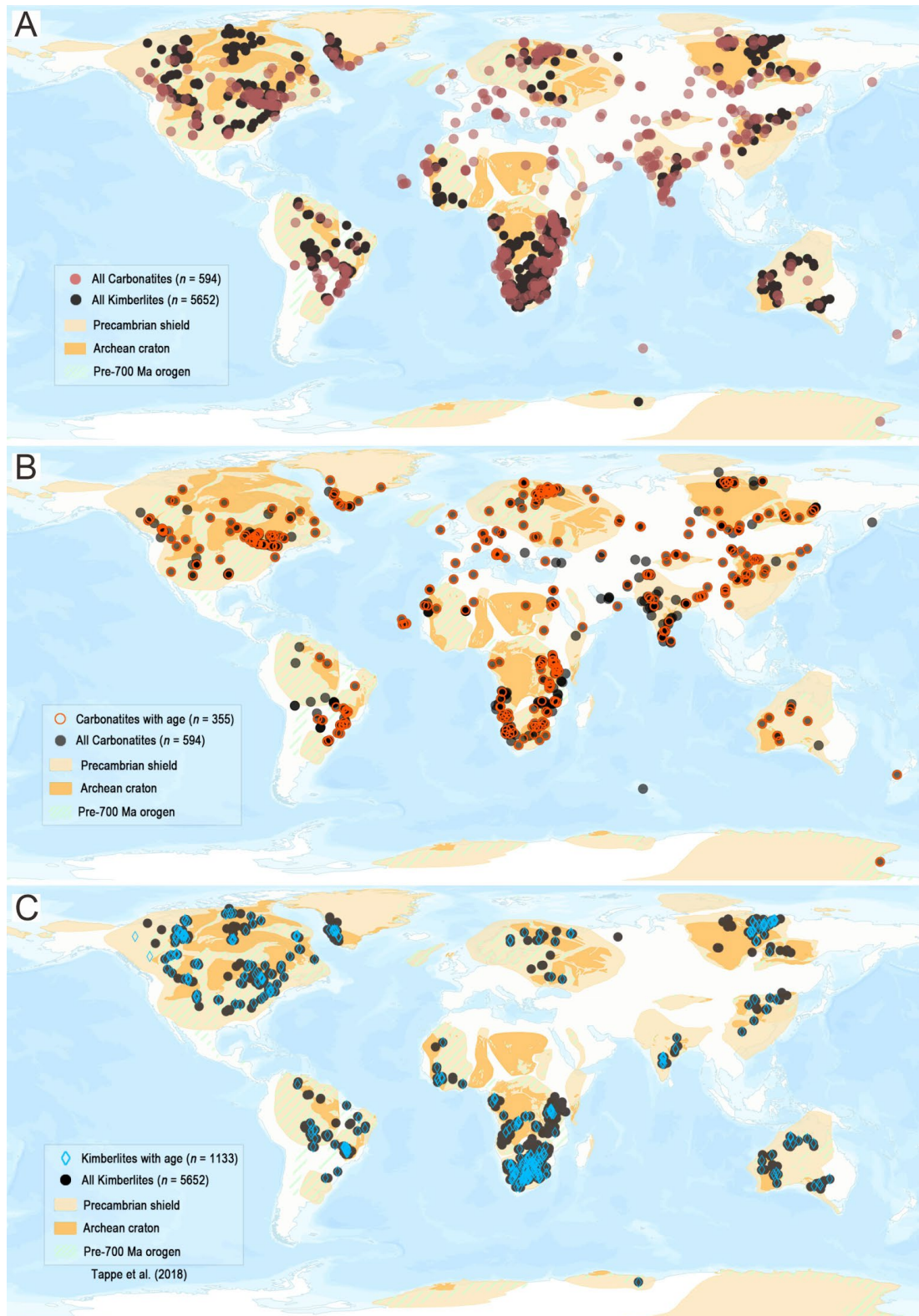


Fig. S2 World map showing carbonatite and kimberlite. (A) Spatial distribution comparison of global carbonatites and kimberlites; (B) Spatial distribution comparison of dated carbonatites and global carbonatites; (C) Spatial distribution comparison of dated kimberlites and global kimberlites. Kimberlites data from [Tappe et al. \(2018\)](#).

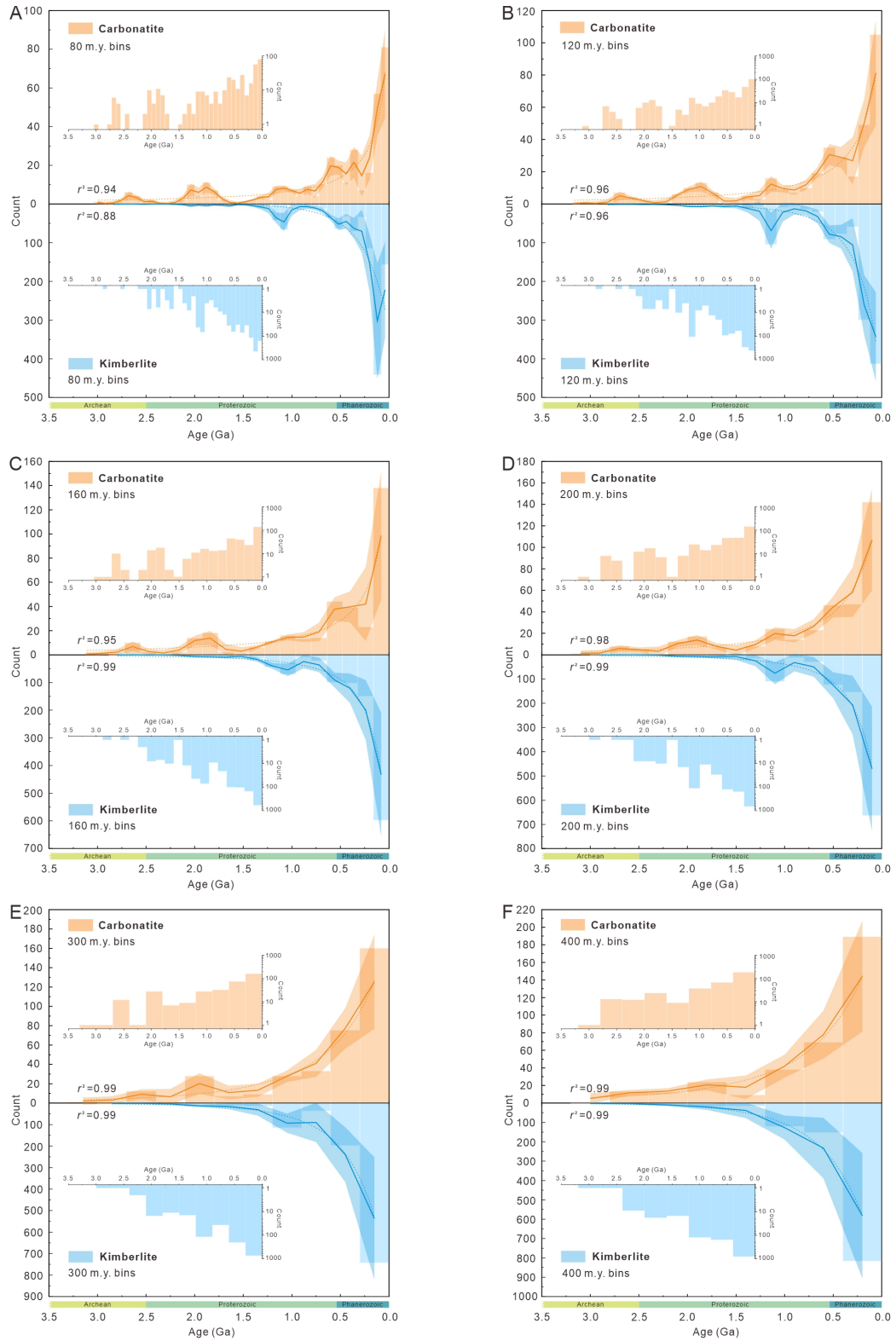


Fig. S3 The age frequency distribution of carbonatites and kimberlites with different bin sizes (A-F, from 80 m.y. to 400 m.y.). The estimated age distribution curves (solid lines; 1σ confidence intervals) were calculated using a locally-estimated scatterplot and bootstrap method in Acycle software (Li et al., 2019). The fitting power functions (dashed lines) were evaluated by r^2 . Insets are with logarithmic scales. Kimberlite data is from Tappe et al. (2018).

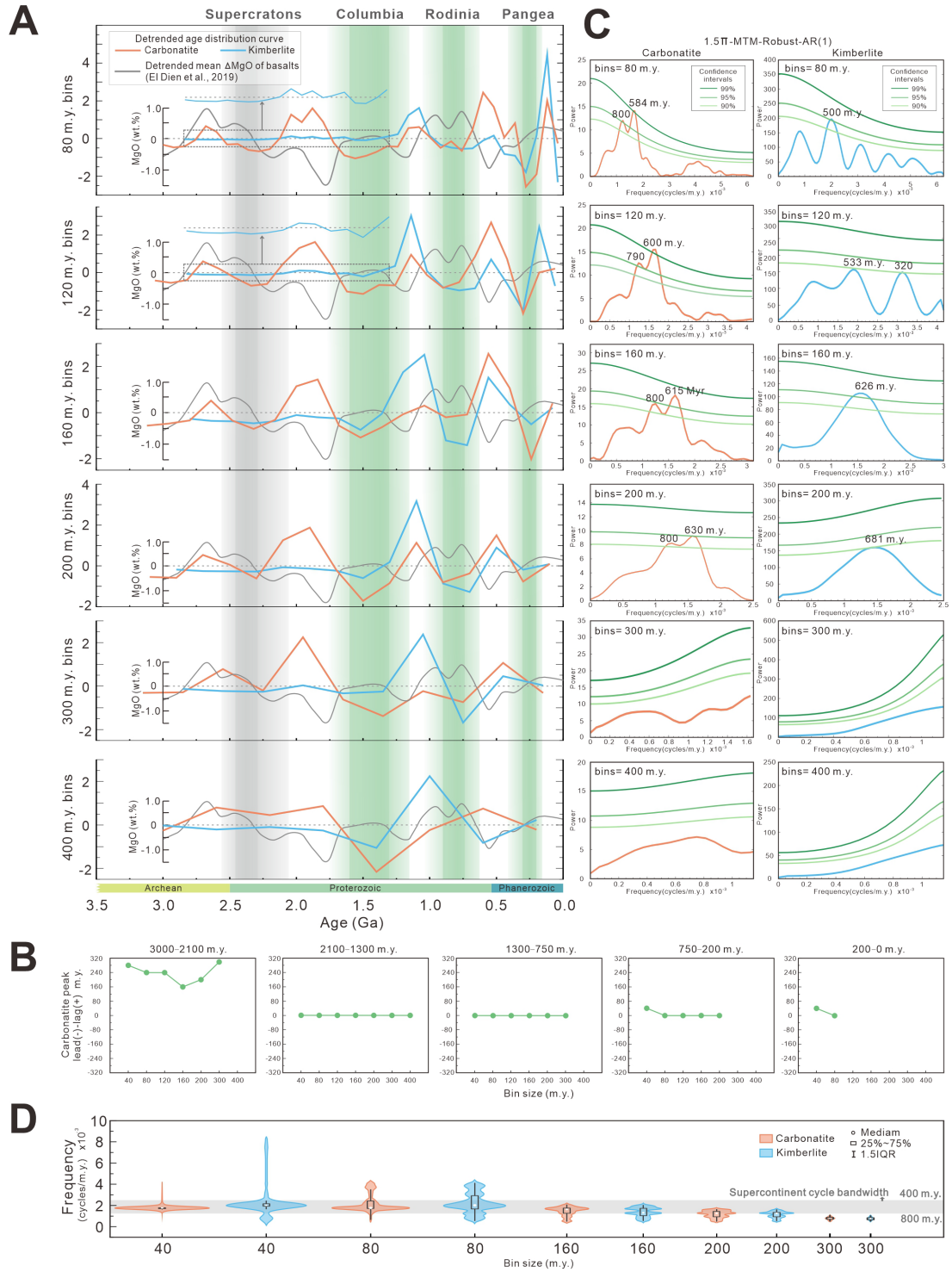


Fig. S4. (A) Detrended carbonatite and kimberlite age distribution curves (z-score) according to different bin sizes compared to the detrended global mean ΔMgO of basalts (grey line, El Dien et al., 2019) and supercontinent/supercraton phases (gray bars; Mitchell et al., 2021). (B) Variation of the lead-lag relationship of detrended carbonatite and kimberlite age distribution curves with bin size selection in the different periods (cases with less than three data in any time period were not calculated). There is a significant change in the interval from 3.0–2.1 Ga, while the results are stable within 80 m.y. in other time intervals. (C) MTM power spectra of detrended carbonatite and

kimberlite age distribution curves according to different bin sizes with confidence levels. (D) Violin plot of frequency above 90% confidence levels given by 10,000 Monte Carlo Simulation combined with MTM for the different bin sizes of carbonatite and kimberlite age distribution curves in 1σ confidence intervals. 400 m.y. bin size has no data available.

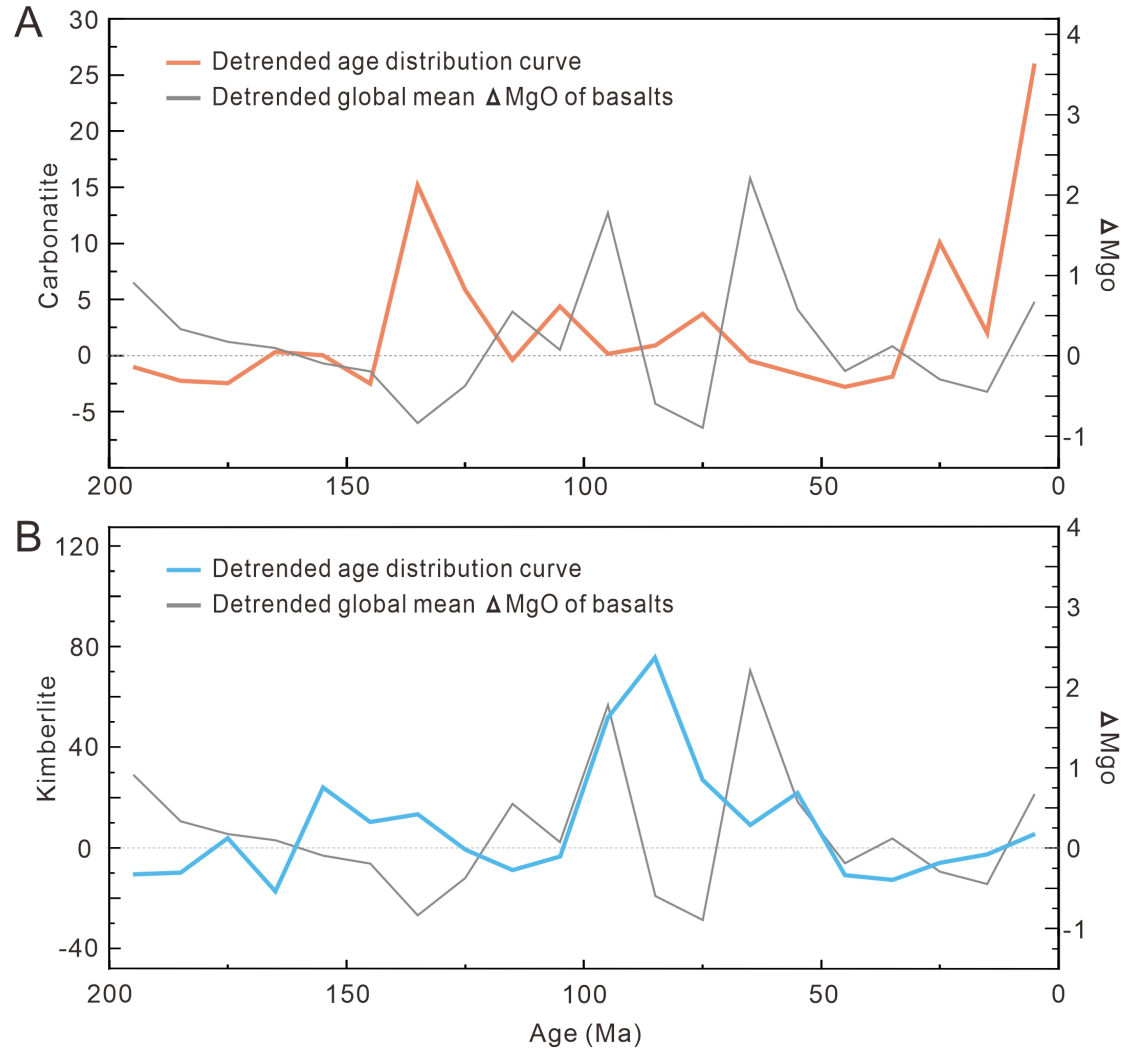


Fig. S5. Detrended carbonatite (A) and kimberlite (B) age distribution curves compare to the detrended global mean ΔMgO of basalts, during 200–0 Ma (raw data, bin size=10 m.y.). MgO data is from [El Dien et al., 2019](#). Detrend their secular trend using rLoess method.

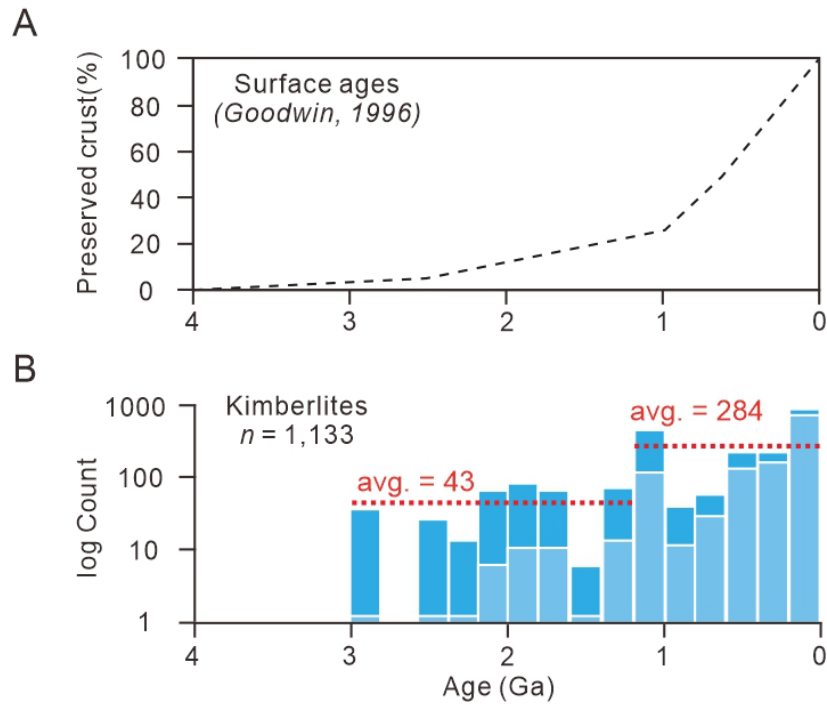


Fig. S6. Kimberlite occurrences taking into account surface preservation. (A) Surface rock ages through time as a proxy for long term erosion of cratons into which kimberlites are predominantly emplaced. (B) Kimberlites occurrences (200 Myr bins and log scale). Light blue, unweighted raw data; dark blue, inversely weighted according to surface preservation (A). Red dashed lines show averages of weighted occurrences indicating that the state shift increase ca. 1.2 Gyr ago remains statistically significant even when preservation is taken into account. The raw kimberlite database is from [Tappe et al. \(2018\)](#).

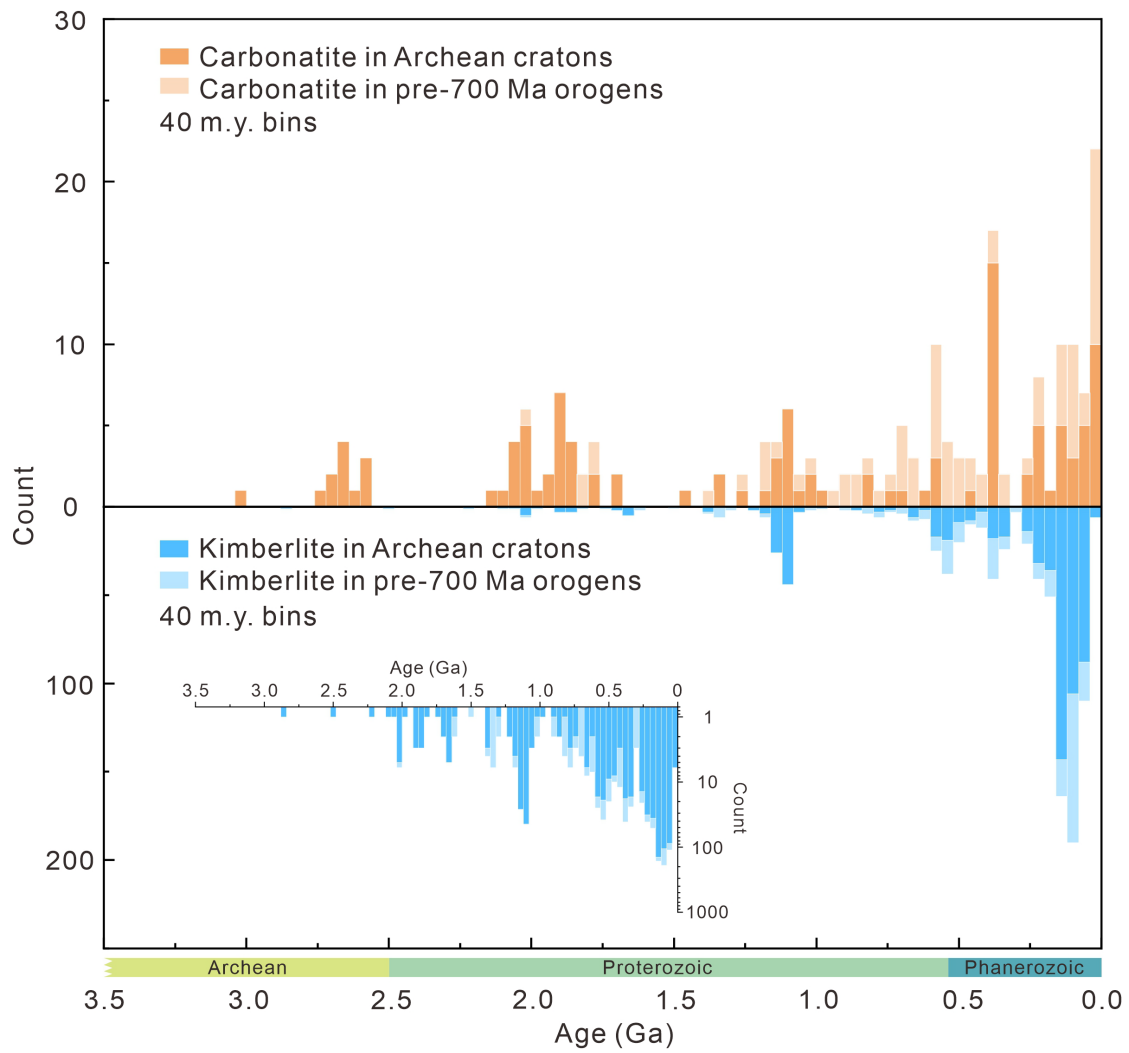


Fig. S7. The stacked age records reflection of carbonatites and kimberlites occurred in the residual Archean cartons or Precambrian orogens. Insets are kimberlite age records plotted on logarithmic scales. Kimberlite database from [Tappe et al. \(2018\)](#).

References Cited

- El Dien, H.G., Doucet, L.S., Li, Z.X., Cox, G., and Mitchell, R., 2019, Global geochemical fingerprinting of plume intensity suggests coupling with the supercontinent cycle: *Nature communications*, v. 10, 5270, <https://doi.org/10.1038/s41467-019-13300-4>.
- Goodwin, A.M., 1996, *Principles of Precambrian geology*: Elsevier.
- Li, M., Hinnov, L.A., and Kump, L.R. 2019. Acycle: Time-series analysis software for paleoclimate projects and education, *Computers & Geosciences*, 127: 12-22. <https://doi.org/10.1016/j.cageo.2019.02.011>.
- Li, X.C., Yang, K.F., Spandler, C., Fan, H.R., Zhou, M.F., Hao, J.L., and Yang, Y.H., 2021, The effect of fluid-aided modification on the Sm-Nd and Th-Pb geochronology of monazite and bastnäsité: Implication for resolving complex isotopic age data in REE ore systems: *Geochimica et Cosmochimica Acta*, v. 300, p 1-24, <https://doi.org/10.1016/j.gca.2021.02.028>.
- Mann, M.E., and Lees, J.M., 1996. Robust estimation of background noise and signal detection in climatic time series. *Climatic Change*, 33, 409-445, <https://doi.org/10.1007/BF00142586>.
- Mitchell, R.N., Zhang, N., Salminen, J., Liu, Y., Spencer, C.J., Steinberger, B., Murphy, T.B., and Li, Z.X., 2021, The supercontinent cycle: *Nature Reviews Earth & Environment*, v. 2, p. 358-374, <https://doi.org/10.1038/s43017-021-00160-0>.
- Tappe, S., Smart, K., Torsvik, T., Massuyeau, M., and de Wit, M., 2018, Geodynamics of kimberlites on a cooling Earth: clues to plate tectonic evolution and deep volatile cycles: *Earth and Planetary Science Letters*, v. 484, p. 1-14, <https://doi.org/10.1016/j.epsl.2017.12.013>.
- Woolley, A.R., and Kjarsgaard, B.A., 2008, Paragenetic types of carbonatite as indicated by the diversity and relative abundances of associated silicate rocks: evidence from a global database: *The Canadian Mineralogist*, v. 46, p. 741-752, <https://doi.org/10.3749/canmin.46.4.741>.
- Yang, K.F., Fan, H.R., Pirajno, F. and Li, X.C., 2019, The Bayan Obo (China) giant REE accumulation conundrum elucidated by intense magmatic differentiation of carbonatite: *Geology*, v. 47, p 1198–1202, <https://doi.org/10.1130/G46674.1>.